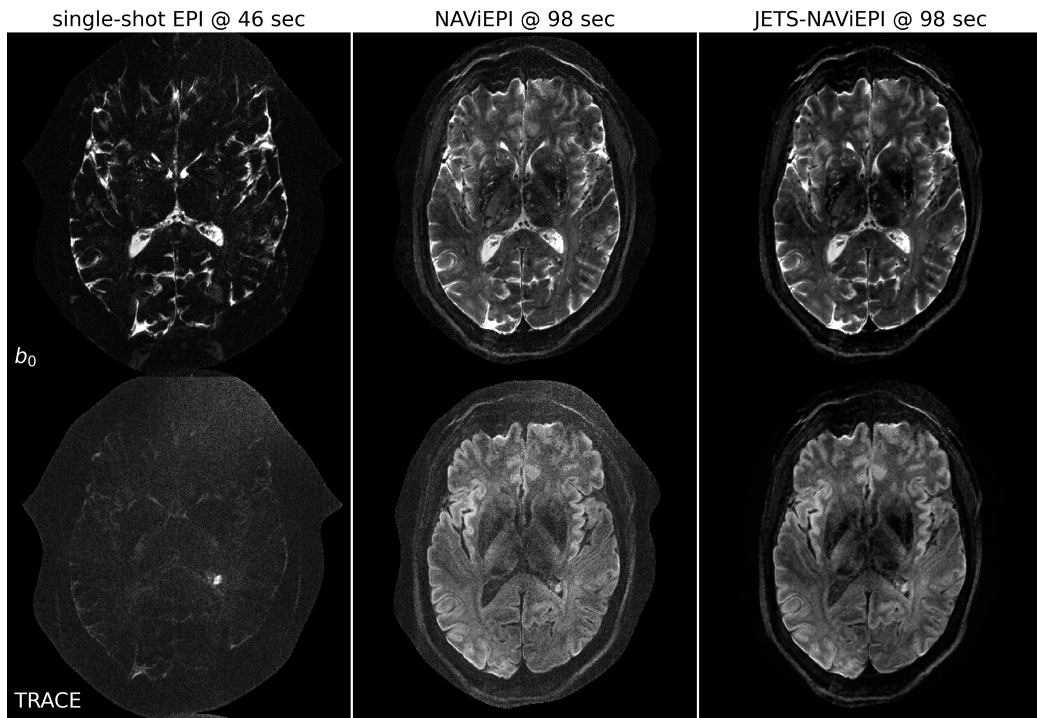


Graphical Abstract

Accelerated Diffusion Weighted Magnetic Resonance Imaging at 7 T: Joint Reconstruction for Shift-Encoded Navigator-based Interleaved Echo Planar Imaging (JETS-NAViEPI)

Zhengguo Tan, Patrick Alexander Liebig, Robin Martin Heidemann, Frederik Bernd Laun, Florian Knoll

3-scan trace acquisition with voxel size 0.5 X 0.5 X 2.0 mm³



Highlights

Accelerated Diffusion Weighted Magnetic Resonance Imaging at 7 T: Joint Reconstruction for Shift-Encoded Navigator-based Interleaved Echo Planar Imaging (JETS-NAViEPI)

Zhengguo Tan, Patrick Alexander Liebig, Robin Martin Heidemann, Frederik Bernd Laun, Florian Knoll

- Navigator-based interleaved EPI acquisition with minimal distortion mismatch between echoes
- Novel accelerated diffusion acquisition with shifted phase encoding among diffusion directions for complementary k - q -space sampling at 7 T
- Generalized joint k - q -slice diffusion-weighted image reconstruction with overlapping locally low-rank regularization
- Efficient simultaneous multi-slice (SMS) image reconstruction
- 3-scan trace acquisition with the voxel size $0.5 \times 0.5 \times 2.0 \text{ mm}^3$ and 60 slices at 1.5 min

Accelerated Diffusion Weighted Magnetic Resonance Imaging at 7 T: Joint Reconstruction for Shift-Encoded Navigator-based Interleaved Echo Planar Imaging (JETS-NAViEPI)

Zhengguo Tan^a, Patrick Alexander Liebig^b, Robin Martin Heidemann^b,
Frederik Bernd Laun^c, Florian Knoll^a

^a*Department Artificial Intelligence in Biomedical Engineering (AIBE),
Friedrich-Alexander University of Erlangen-Nuremberg, Erlangen, Germany*

^b*Siemens Healthcare GmbH, Erlangen, Germany*

^c*Institute of Radiology, University Hospital Erlangen, Friedrich-Alexander University of Erlangen-Nuremberg, Erlangen, Germany*

Abstract

The pursuit of high spatial-angular-temporal resolution for in vivo diffusion-weighted magnetic resonance imaging (DW-MRI) at ultra-high field strength (7 T and above) is important in understanding brain microstructure and function. Such pursuit, however, faces several technical challenges. First, increased off-resonance and shorter T_2 relaxation require faster echo train readouts. Second, existing high-resolution DW-MRI techniques usually employ in-plane fully-sampled multi-shot EPI, which not only prolongs the scan time but also induces a high specific absorption rate (SAR) at 7 T. To address these challenges, we develop in this work navigator-based interleaved EPI (NAViEPI) which enforces the same effective echo spacing (ESP) between the imaging and the navigator echo. First, NAViEPI renders no distortion mismatch between the two echoes, and thus simplifies shot-to-shot phase variation correction. Second, NAViEPI allows for a large number of shots

(e.g. > 4) with undersampled iEPI acquisition, thereby rendering clinically-feasible high-resolution sub-millimeter protocols. To retain signal-to-noise ratio (SNR) and to reduce undersampling artifacts, we developed a k_y -shift encoding among diffusion encodings to explore complementary k - q -space sampling. Moreover, we developed a novel joint reconstruction with overlapping locally low-rank regularization generalized to the multi-band multi-shot acquisition at 7 T (dubbed JETS-NAViEPI). Our method was demonstrated with experimental results covering 1 mm isotropic resolution multi b -value DWI and sub-millimeter in-plane resolution fast TRACE acquisition.

Keywords: Diffusion-weighted magnetic resonance imaging, Echo planar imaging, Navigator, Ultra-high field, Joint reconstruction, Low rank, Simultaneous multi slice

¹ **1. Introduction**

² Diffusion-weighted magnetic resonance imaging (DW-MRI) ([Le Bihan et al., 1986; Merboldt et al., 1985](#)) is a non-invasive modality that is sensi-
³ tive to the intravoxel Brownian motion of water molecules. DW-MRI forms
⁴ the basis for diffusion tensor imaging (DTI) ([Basser et al., 1994; Mori et al., 1999](#)) and high angular resolution diffusion imaging (HARDI) ([Tuch et al., 2002](#)), and has been widely used in acute brain ischemia diagnosis, in tumor
⁵ detection and staging, and in neuroscience ([Jones, 2010](#)).

⁶ For DW-MRI acquisition, the commonly used pulse sequence is single-
⁷ shot echo-planar imaging (SS-EPI) ([Mansfield, 1977](#)). SS-EPI is capable of
⁸ rapidly acquiring one DW image per radio-frequency excitation at the order
⁹ of 100 ms, and is thus motion robust. However, conventional SS-EPI, even
¹⁰ with three-fold accelerated acquisition ([Bammer et al., 2001](#)) using parallel
¹¹ imaging ([Roemer et al., 1990; Ra and Rim, 1993; Pruessmann et al., 1999](#);
¹² [Griswold et al., 2002](#)), still suffers from low spatial resolution and geometric
¹³ distortions.

¹⁴ In the quest for high spatial-angular-temporal-resolution and minimal-
¹⁵ geometry-distortion DW-MRI, tremendous efforts have been made. Tech-
¹⁶ niques for the correction of image distortions induced by off-resonances and
¹⁷ eddy currents have been developed ([Andersson et al., 2003](#)). Furthermore,
¹⁸ gSlider ([Setsompop et al., 2018](#)) with blipped-CAIPI ([Setsompop et al., 2012](#))
¹⁹ for simultaneous multi-slice (SMS) ([Maudsley, 1980; Breuer et al., 2005](#))
²⁰ was proposed to achieve high-resolution DW-MRI. Advanced pulse sequences
²¹ based on multi-shot EPI have also been developed, including but not limited
²² to interleaved EPI (iEPI) ([Butts et al., 1993](#)), PROPELLER ([Pipe et al., 2004](#)),

26 2002), and readout-segmented EPI (rsEPI) (Porter and Heidemann, 2009;
27 Heidemann et al., 2010).

28 Based on four-shot iEPI, multiplexed sensitivity encoding (MUSE) image
29 reconstruction achieved DW-MRI with a sub-millimeter in-plane resolution
30 and maximal b -value 800 s/mm^2 at 3 T (Chen et al., 2013). The four-shot
31 iEPI employed in MUSE acquired an in-plane fully-sampled k -space, except
32 partial Fourier. Every shot (segment), corresponding to four-fold under-
33 sampling, was then reconstructed via parallel imaging to obtain shot-to-shot
34 phase variation. This indicates that increasing the number of shots in MUSE
35 will result in higher undersampling per shot, and consequently, degrade shot
36 phase estimation (Wu and Miller, 2017).

37 Alternatively, navigator-based iEPI acquisition has been proposed (Jeong
38 et al., 2013; Dai et al., 2017, 2018). These proposals allow for a larger num-
39 ber of shots, and hence higher spatial resolution. However, due to the use of
40 different ESP between the imaging echo and the navigator echo, these pro-
41 posals suffered from geometric distortion mismatch between the two echoes
42 and thus required specific compensation methods. In contrast, rsEPI (Porter
43 and Heidemann, 2009; Heidemann et al., 2010) used the same readout seg-
44 ment for both echoes, and thus required no distortion correction of navigator
45 echoes.

46 Beyond the MUSE-type parallel imaging reconstruction, compressed sens-
47 ing (Lustig et al., 2007; Block et al., 2007) has been explored. For instance,
48 multi-shot reconstruction techniques based on structured low-rank matrix
49 completion (MUSSELS) (Mani et al., 2017; Bilgic et al., 2019) achieved 5-
50 shot DW-MRI with 9-fold undersampling per shot. Recently, JULEP (Dai

51 et al., 2023) incorporated explicit phase mapping into MUSSELS. These re-
52 construction techniques, i.e., MUSE, MUSSELS and JULEP, targeted the
53 reconstruction of one DW image from interleaved EPI acquisition, and did
54 not explore joint- k - q -space undersampling or reconstruction.

55 Joint- k - q -space undersampling can be achieved via proper regularization
56 along the diffusion encoding direction. Relevant examples are diffusion un-
57 dersampling with Gaussian process estimated reconstruction (DAGER) (Wu
58 et al., 2019) and magnitude-based spatial-angular locally low-rank regular-
59 ization (SPA-LLR) (Hu et al., 2020). However, DAGER addressed the re-
60 construction problem of single-shot EPI acquisition and SPA-LLR focused
61 on the reconstruction of single-band and fully-sampled iEPI acquisition.

62 In this work, we propose a Joint k - q -slice rEconsTruction framework
63 for Shift-encoded NAVigator-based interleaved EPI at 7 T (dubbed JETS-
64 NAViEPI). Our pulse sequence, NAViEPI, differs from most existing tech-
65 niques. First, NAViEPI builds upon interleaved EPI, thereby allowing for
66 fast and efficient k -space coverage. Second, inspired by rsEPI, NAViEPI en-
67 sures the same effective ESP between the imaging and the navigator echo,
68 thereby minimizing geometric distortion and allowing for the use of a larger
69 number of shots. NAViEPI essentially integrates the advantages of both iEPI
70 and rsEPI. Third, NAViEPI utilizes undersampled multi-shot iEPI, thereby
71 alleviating the SAR problem at 7 T. Fourth, NAViEPI shifts the k -space in-
72 plane sampling pattern along the phase encoding (k_y) direction. This shifting
73 creates complementary k - q -space sampling, which leads to the possibility of
74 our joint k - q -slice reconstruction. Specifically, we employ spatial-diffusion
75 overlapping LLR regularization to jointly reconstruct all diffusion encodings

⁷⁶ and multi-band slices. In vivo experiments at 7 T and comparisons with other
⁷⁷ techniques demonstrate the efficiency of our proposed method in achieving
⁷⁸ high spatial resolution DW-MRI at ultra-high field.

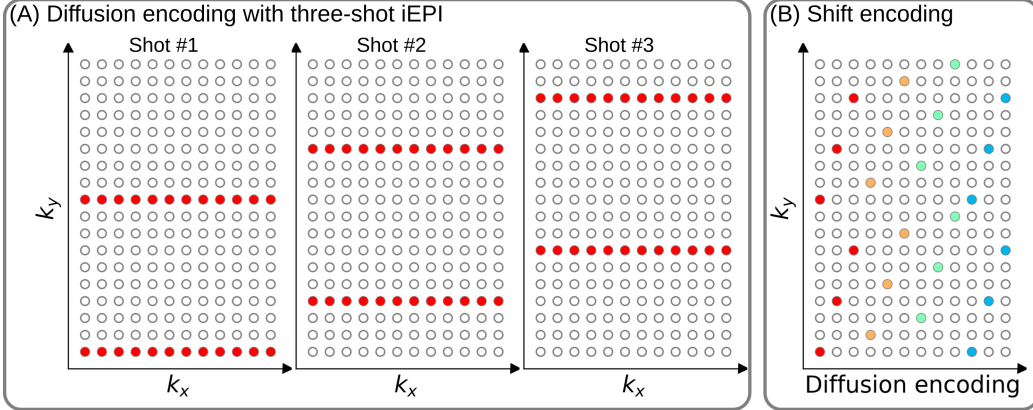


Figure 1: (A) An example DW-MRI acquisition with three-shot interleaved EPI acquisition. (B) The proposed k_y shifted diffusion encoding scheme. This example employs three shots per DW image. Therefore, every three columns have the same color.

⁷⁹ **2. Materials and methods**

⁸⁰ *2.1. Multi-band shift-encoded iEPI acquisition*

⁸¹ Fig. 1 (A) displays the diffusion-weighted image acquisition based on
⁸² three-shot interleaved EPI with three-fold in-plane undersampling. Conven-
⁸³ tionally, such a sampling pattern is repeated for all diffusion directions. In
⁸⁴ contrast, we propose the k_y -shifted diffusion encoding, as shown in Fig. 1 (B).
⁸⁵ The interleaved EPI sampling pattern is shifted by one k_y line per diffusion
⁸⁶ direction, with the cycling period being the in-plane undersampling factor.

⁸⁷ It is worth noting that, as shown in Fig. 1 (A), the undersampling factor
⁸⁸ of one segment is $R_{\text{in-plane}} \times N_{\text{shot}}$ (ignore multi-band undersampling here),
⁸⁹ yielding nine-fold in-plane undersampling in this example. In other words,
⁹⁰ the undersampling factor per segment linearly scales up with the number
⁹¹ of shots. Consequently, conventional self-gating reconstruction techniques,
⁹² e.g. MUSE, suffer from degraded shot-to-shot phase estimation, which in

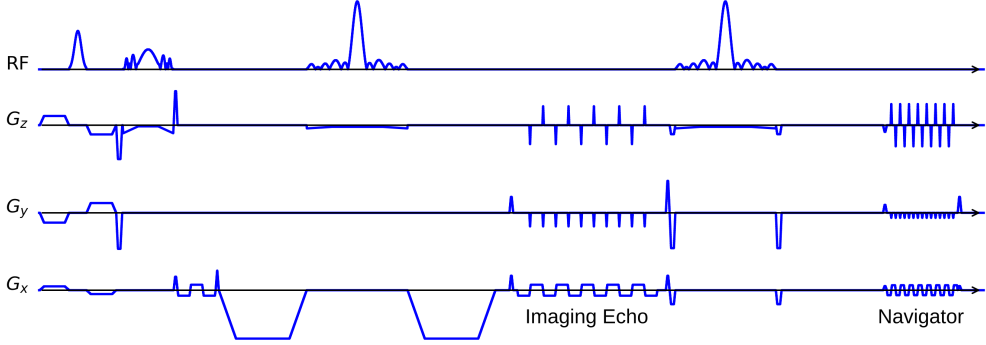


Figure 2: The NAViEPI sequence diagram. SMS is utilized for the acquisition of both imaging and navigator echoes. While the acceleration factor per navigator is the same as listed in Table 1, the acceleration factor per imaging echo is in addition linearly scaled by the number of shots.

93 turn limits the number of shots and spatial resolution.

94 *2.2. NAViEPI: Navigator-based iEPI with consistent effective ESP between
95 the imaging and the navigator echo - where iEPI meets rsEPI*

96 Instead of the self-gated MUSE with in-plane fully-sampled iEPI and
97 a limited number of shots, We propose NAVigator-based interleaved EPI
98 (NAViEPI), as illustrated in Fig. 2. Inspired by rsEPI (Porter and Hei-
99 demann, 2009), NAViEPI enforces a consistent effective ESP between the
100 imaging and the navigator echo, thereby minimizing distortion mismatch
101 between the two echoes.

102 Since one imaging echo presents one segment in multi-shot EPI acquisi-
103 tion, its effective ESP is defined as

$$\text{ESP}_{\text{eff}} = \frac{\text{ESP}}{R_{\text{in-plane}} \times N_{\text{shot}}} \quad (1)$$

104 Here, a larger number of shots (segments) increases the undersampling factor
105 per segment (see Fig. 1), but decreases the effective ESP. Since the navigator

106 echo is acquired for each segment, its in-plane undersampling factor equals
107 $R_{\text{in-plane}}$. Therefore, the effective ESP of the navigator echo must match that
108 of the imaging echo, as given in Eq. (1). With a matching effective ESP, the
109 base resolution of the navigator echo can then be determined.

110 *2.3. In vivo acquisition protocols*

111 We implemented multiple in-vivo acquisition protocols at a clinical 7 T
112 MR system (MAGNETOM Terra, Siemens Healthineers, Erlangen, Ger-
113 many) equipped with a 32-channel head coil (Nova Medical, Wilmington,
114 MA, USA) and the XR-gradient system (maximum gradient strength 80 mT/m
115 with a peak slew rate of 200 T/m/s). To calibrate coil sensitivity maps, refer-
116 ence scans employed a gradient-echo (GRE) sequence. Spectral fat saturation
117 and mono-polar diffusion-encoding gradients were used. The phase-encoding
118 direction was selected as anterior-to-posterior.

Table 1: NAViEPI acquisition protocols

Protocol	1.0 mm isotropic		sub-millimeter	
	#1	#2	#3	#4
Diffusion mode	MDDW ⁽¹⁾		3-scan trace	
Diffusion scheme	monopolar			
Diffusion direction	20	114	3	
<i>b</i> -value (s/mm ²)	1000	3-shell ⁽²⁾	1000	
<i>b</i> ₀	0	12	1	
FOV (mm ²)	200	214	220	
In-plane resolution (mm ²)	1.0		0.5	
Slice thickness (mm)	1.0		2.0	
Slices	141	114	60	
Navigator	No	No	Yes	No
Shots	4	2	5	1
TR (ms)	7700	5200	4400	8000
TEs (ms)	67	66	58/95.1	143
ESP (ms)	1.02	0.81	1.52	1.48
Bandwidth (Hz/Pixel)	1086	1460	758	
Partial Fourier			6/8	
Acceleration ⁽³⁾	1 × 3	3 × 3	3 × 2	
TA (min) ⁽⁴⁾	10 : 42	22 : 25	1 : 38	0 : 46

⁽¹⁾ MDDW: Multi-direction diffusion weighting;

⁽²⁾ 3-shell: 20, 30, and 64 directions with *b*-values of 1000, 2000, and 3000 s/mm², respectively;

⁽³⁾ Acceleration: Both in-plane and slice undersampling can be employed, denoted as (*R*_{in-plane} × *R*_{slice});

⁽⁴⁾ TA: Total acquisition time.

120 This study was approved by the local ethics committee. Three volunteers
121 with informed consent obtained before scanning participated in this study.
122 Detailed acquisition protocols are listed in Table 1. In the spirit of repro- R989.1
123ducible research, another volunteer with informed consent was recruited for
124 the scan of all acquisition protocols, and the results were displayed in Sup-
125 plementary Information.

126 *2.3.1. 20-diffusion-direction acquisition at 1 mm isotropic resolution*

127 As listed in Table 1, Protocol #1 with four-shot iEPI and without in-
128 plane undersampling was implemented. This protocol represents the acquisi-
129 tion scheme employed in many existing multi-shot reconstruction techniques,
130 (e.g., MUSE, SPA-LLR, and JULEP). The acquired data from this protocol
131 served as ground truth. Different reconstruction methods, specifically JETS,
132 MUSE, and JULEP were compared. We compared with JULEP instead of
133 MUSSELS, because JULEP uses not only structured low-rank constraints
134 but also explicit phase mapping.

135 We then retrospectively reduced the four-shot data to only one shot per
136 diffusion encoding without and with the proposed k_y shifting to simulate
137 four-fold in-plane undersampling. JETS reconstruction was performed on
138 the fully-sampled data and the retrospectively undersampled data to validate
139 the proposed k_y -shifted acquisition.

140 *2.3.2. Three-shell acquisition at 1 mm isotropic resolution*

141 Protocol #2 in Table 1 was implemented for multi-shell diffusion tensor
142 imaging (DTI) (Basser et al., 1994). We acquired a total of 114 diffusion
143 directions, whereas b_0 measurements were interspersed every ten diffusion

₁₄₄ directions. This protocol was used to demonstrate the capability of JETS
₁₄₅ in achieving high spatial-angular-temporal resolution.

₁₄₆ *2.3.3. 3-scan trace acquisition at $0.5 \times 0.5 \times 2.0 \text{ mm}^3$ voxel size*

₁₄₇ As listed in Table 1, Protocol #3 was implemented based on NAViEPI
₁₄₈ with five shots per diffusion encoding. This protocol was compared against
₁₄₉ single-shot EPI (Protocol #4) with the same spatial resolution and acceler-
₁₅₀ ation, such as to demonstrate the sampling efficiency of NAViEPI.

₁₅₁ *2.4. Forward modeling*

₁₅₂ Our proposed acquisition method yields multi-dimensional multi-band
₁₅₃ k -space data $\mathbf{y}_{c,q,s}$, where c, q, s denotes the index of the coil sensitivity
₁₅₄ map, the diffusion encoding, and the shot, respectively. Acquisition modeling
₁₅₅ needs to consider several aspects.

₁₅₆ First, the acquired k -space data \mathbf{y} is mapped from individual shot images
₁₅₇ $\mathbf{x}_{q,s,z}$ via the forward model,

$$\begin{aligned} \mathbf{y}_{c,q,s} &= \mathbf{P}_{q,s} \boldsymbol{\Sigma} \boldsymbol{\Theta}_z \mathbf{F} \mathbf{S}_c \mathbf{x}_{q,s,z} \\ \mathbf{y} &:= \mathbf{E}_1 \mathbf{x} \end{aligned} \quad (2)$$

₁₅₈ Here, the encoding matrix \mathbf{E}_1 comprises a chain of linear operators. Every
₁₅₉ shot image \mathbf{x} is point-wise multiplied by a set of coil sensitivity maps (\mathbf{S}) and
₁₆₀ Fourier transformed (\mathbf{F}). The output is then point-wise multiplied by the
₁₆₁ multi-slice phase map ($\boldsymbol{\Theta}$) with z the slice index in simultaneously excited
₁₆₂ slices. This operator shifts individual slice along the phase-encoding direction
₁₆₃ via varying phase modulation (Breuer et al., 2005). The SMS k -space data

164 is then summed (collapsed, Σ) along the slice dimension and masked (point-
165 wise multiplied, \mathbf{P}) by the sampling pattern of each diffusion encoding and
166 shot.

167 Second, for diffusion MRI based on multi-shot EPI, multiple shots ac-
168 quired for a given diffusion encoding need to be combined as one DW image
169 ($\tilde{\mathbf{x}}$). One possibility is to perform magnitude average (Chen et al., 2013)
170 or root-sum-squares (RSS) (Mani et al., 2017) of shot images. This method
171 is robust to in-plane motion, but sub-optimal concerning SNR (Guhaniyogi
172 et al., 2016). Alternatively, shot combination can be done via shot-to-shot
173 phase variation correction (Liu et al., 2005; Chen et al., 2013). This can be
174 incorporated into our formulation as point-wise multiplication between the
175 shot-to-shot phase variation (Φ) and the DW image ($\tilde{\mathbf{x}}$),

$$\mathbf{x}_{q,s,z} = \Phi_{q,s,z} \tilde{\mathbf{x}}_{q,z} \quad (3)$$

176 Note that $\tilde{\mathbf{x}}$ can be obtained by applying the adjoint of Φ to \mathbf{x} . In MUSE,
177 Φ is obtained by parallel imaging reconstruction of all shots with subsequent
178 phase smoothing of every shot image. Based on this phase correction, the
179 complete forward model follows

$$\mathbf{y} := \mathbf{E}_2 \tilde{\mathbf{x}} = \mathbf{E}_1 \Phi \tilde{\mathbf{x}} \quad (4)$$

180 where the encoding matrix \mathbf{E}_2 comprises the chain of the shot-to-shot phase
181 variation Φ and the encoding matrix \mathbf{E}_1 . We implemented these two encoding
182 operators in SigPy (Ong and Lustig, 2019).

183 2.5. Joint k - q -slice reconstruction

184 Based on the generalized forward models in Eqs. (2) and (4), our proposed
185 joint k - q -slice reconstruction can be formulated as a three-step approach.

186 **I. Navigator echo reconstruction.** The acquisition of navigator echoes
 187 follows the forward model in Eq. (2), so the reconstruction of navigator
 188 echoes can be formulated as:

$$\operatorname{argmin}_{\mathbf{x}} \|\mathbf{y} - \mathbf{E}_1 \mathbf{x}\|_2^2 + \lambda \mathbf{R}(\mathbf{x}) \quad (5)$$

189 where $\mathbf{R}(\mathbf{x})$ denotes the regularization functional with the regularization
 190 strength λ . In this work, ℓ^2 regularization was used, i.e., $\mathbf{R}(\mathbf{x}) =$
 191 $\|\mathbf{x}\|_2^2$. In the case of self-navigating (i.e., no navigator acquired) as
 192 Protocol #2, the central k -space region (i.e., 1/4 of the full image matrix)
 193 of each segment is used as \mathbf{y} in Eq. (5).

194 **II. Iterative phase smoothing.** Shot-to-shot phase variation was ex-
 195 tracted from the reconstructed navigator echo phases. Assuming that
 196 phase images are spatially smooth (Chen et al., 2013; Dai et al., 2023),
 197 we employed the iterative approach to smooth phase,

$$\mathbf{x}^{(k+1)} = \mathbf{F}^{-1} \mathcal{H} \mathbf{F} \mathbf{x}^{(k)} \quad (6)$$

198 where the index k denotes the phase smoothing iteration step, and $x^{(0)}$
 199 is then the reconstructed navigator image from Step I. \mathcal{H} is the Hanning
 200 window.

201 **III. Shot-combined reconstruction.** Joint reconstruction of all DW im-
 202 ages using the shot-combined forward model \mathbf{E}_2 with shot-to-shot phase
 203 variation from Step II reads:

$$\operatorname{argmin}_{\tilde{\mathbf{x}}} \|\mathbf{y} - \mathbf{E}_2 \tilde{\mathbf{x}}\|_2^2 + \lambda \|\mathbf{T}(\tilde{\mathbf{x}})\|_* \quad (7)$$

204 Here, LLR regularization was employed in the local spatial-diffusion
 205 matrices, based on the theory of partially separable functions (Liang,

206 2007; Trzasko and Manduca, 2011; Zhang et al., 2015). \mathbf{T} represents
207 a linear operator that firstly slides a local patch window through all
208 DW images and then flattens every set of local patches to construct
209 two-dimensional (2D) spatial-diffusion matrices. The spatial dimension
210 equals the block size, and the diffusion dimension is the number of dif-
211 fusion encodings. $\|\mathbf{T}(\tilde{\mathbf{x}})\|_*$ is the nuclear norm, i.e. the sum of singular
212 values of a spatial-diffusion matrix. This nuclear norm regularization
213 was accomplished via singular value thresholding (SVT) of each spatial-
214 diffusion matrix (Cai et al., 2010). After SVT, the adjoint of \mathbf{T} , \mathbf{T}^H ,
215 was needed to reorder pixel values from the spatial-diffusion matrices
216 back to DW images. To alleviate checkerboard artifacts induced by
217 LLR regularization with non-overlapping blocks (Hu et al., 2020), we
218 employed overlapping blocks. In this case, values from overlapping po-
219 sitions are summed up to the output of \mathbf{T}^H . To enable the correct use
220 of \mathbf{T}^H , we element-wise divided the output of \mathbf{T}^H by a scaling matrix.
221 This matrix was obtained via $\mathbf{T}^H(\mathbf{T}(\mathbf{1}))$, where $\mathbf{1}$ denotes the matrix
222 of all ones with the same shape as the input \mathbf{x} .

223 2.6. Reconstruction

224 The acquired raw data was read in by twixtools (<https://github.com/pehses/twixtools>). Ramp-sampling regridding and FOV/2-ghost correc-
225 tion were also performed in twixtools. Subsequently, coil sensitivity maps
226 were computed from reference scans using ESPIRiT (Uecker et al., 2014) in
227 SigPy (Ong and Lustig, 2019).

228 With this pre-processing as well as the implemented forward models and
229 proximal operator, the inverse problem in Eq. (7) was solved by the alter-

231 nating direction method of multipliers (ADMM) (Boyd et al., 2010).

232 ADMM solves the minimization problems in an alternating update scheme,

$$\begin{cases} \mathbf{x}^{(k+1)} := \underset{\mathbf{x}}{\operatorname{argmin}} \| \mathbf{y} - \mathbf{E}(\mathbf{x}) \|^2 + \rho/2 \| \mathbf{T}\mathbf{x} - \mathbf{z}^{(k)} + \mathbf{u}^{(k)} \|_2^2 \\ \mathbf{z}^{(k+1)} := \mathcal{T}_{\lambda/\rho}(\mathbf{T}\mathbf{x}^{(k+1)} + \mathbf{u}^{(k)}) \\ \mathbf{u}^{(k+1)} := \mathbf{u}^{(k)} + \mathbf{T}\mathbf{x}^{(k+1)} - \mathbf{z}^{(k+1)} \end{cases} \quad (8)$$

233 where k denotes the ADMM iteration. \mathbf{z} is the auxiliary variable ($\mathbf{z} = \mathbf{T}\mathbf{x}$),
234 and \mathbf{u} is the Lagrangian multipliers. Importantly, when solving Eq. (2), \mathbf{x}
235 denotes shot images and \mathbf{E} denotes \mathbf{E}_1 in Eq. (8). In contrast, \mathbf{x} denotes shot-
236 combined images and \mathbf{E} denotes \mathbf{E}_2 when solving Eq. (4). \mathbf{x} can be solved
237 using linear least square algorithms, e.g. conjugate gradients (Hestenes and
238 Stiefel, 1952), while \mathbf{z} is updated via singular value thresholding (\mathcal{T}) with
239 the thresholding parameter λ/ρ . The coupling parameter ρ is effective in
240 both the update of \mathbf{x} and \mathbf{z} . It acts as Tikhonov regularization strength
241 when updating \mathbf{x} , but also inversely scales the thresholding strength when
242 updating \mathbf{z} .

243 In this work, 15 ADMM iterations with $\rho = 0.05$ and $\lambda = 0.08$ were used.

244 All reconstructions were done on a single A100 SXM4/NVLink GPU with
245 40 GB memory (NVIDIA, Santa Clara, CA, USA).

246 We compared our proposed joint reconstruction with established multi-
247 shot reconstruction techniques, specifically, MUSE (Chen et al., 2013) and
248 JULEP (Dai et al., 2023), hosted on GitHub by Dr. Dai (Dai et al., 2023).
249 Further, we performed the local-PCA denoising (Cordero-Grande et al., 2019)
250 as implemented in MRtrix (Tournier et al., 2019) on the MUSE reconstructed
251 complex DW images.

252 The in vivo data acquired from Protocol #2 in Table 1 consisted of 126

253 diffusion directions, which exceeds the available GPU memory. Therefore,
254 the 126 data volumes were uniformly split into three parts for our JETS
255 reconstruction with a LLR block width of 6 and the LLR regularization in
256 both Steps I and III in Section 2.5. In addition, MUSE reconstruction was
257 also performed, followed by the local-PCA denoising. Reconstructed DWIs
258 were then processed by DiPy ([Garyfallidis et al., 2014](#)) to obtain color-coded
259 fractional anisotropy (cFA) maps.

260 **3. Results**

261 *3.1. Iterative smoothing of shot-to-shot phase variation*

262 Navigators were acquired with the acceleration rate as listed in Table 1.
263 Besides, the base resolution of navigators (e.g. 32 in Protocol #3 in Table 1)
264 was smaller than imaging echoes. As a result, reconstructed navigator phases
265 (refer to the first column in Fig. 3) from Step I in Section 2.5 are not spatially
266 smooth. Such phases, when used in the shot-combined reconstruction, result
267 in signal void artifacts in DW images. To address this problem, we utilized
268 the iterative smoothing procedure. As shown in Fig. 3, the ripple-like phase
269 artifact disappears after five iterations. It can also be seen that such an
270 iterative procedure retains the shot-to-shot phase variation.

271 *3.2. Comparison to MUSE and JULEP with four-shot iEPI acquisition*

272 The iterative phase smoothing was also applicable to MUSE-type self-
273 navigating reconstruction, where shot phases were reconstructed from imag-
274 ing echoes. Fig. 4 compares our proposed JETS with MUSE (Chen et al.,
275 2013), MUSE with complex-valued local-PCA denoiser (Cordero-Grande et al.,
276 2019), and JULEP (Dai et al., 2023). The residual noise from MUSE can be
277 largely removed by the denoiser. However, when compared to JETS, the de-
278 noiser shows residual noise patterns within the globus pallidus (indicated by
279 the red arrow). JETS also shows better denoising than JULEP. The reason
280 is that JETS enforces spatial-diffusion regularization, whereas JULEP for-
281 mulates structured low-rank regularization of the four shots for one diffusion
282 encoding.

Iterative smoothing of shot-to-shot phase variation

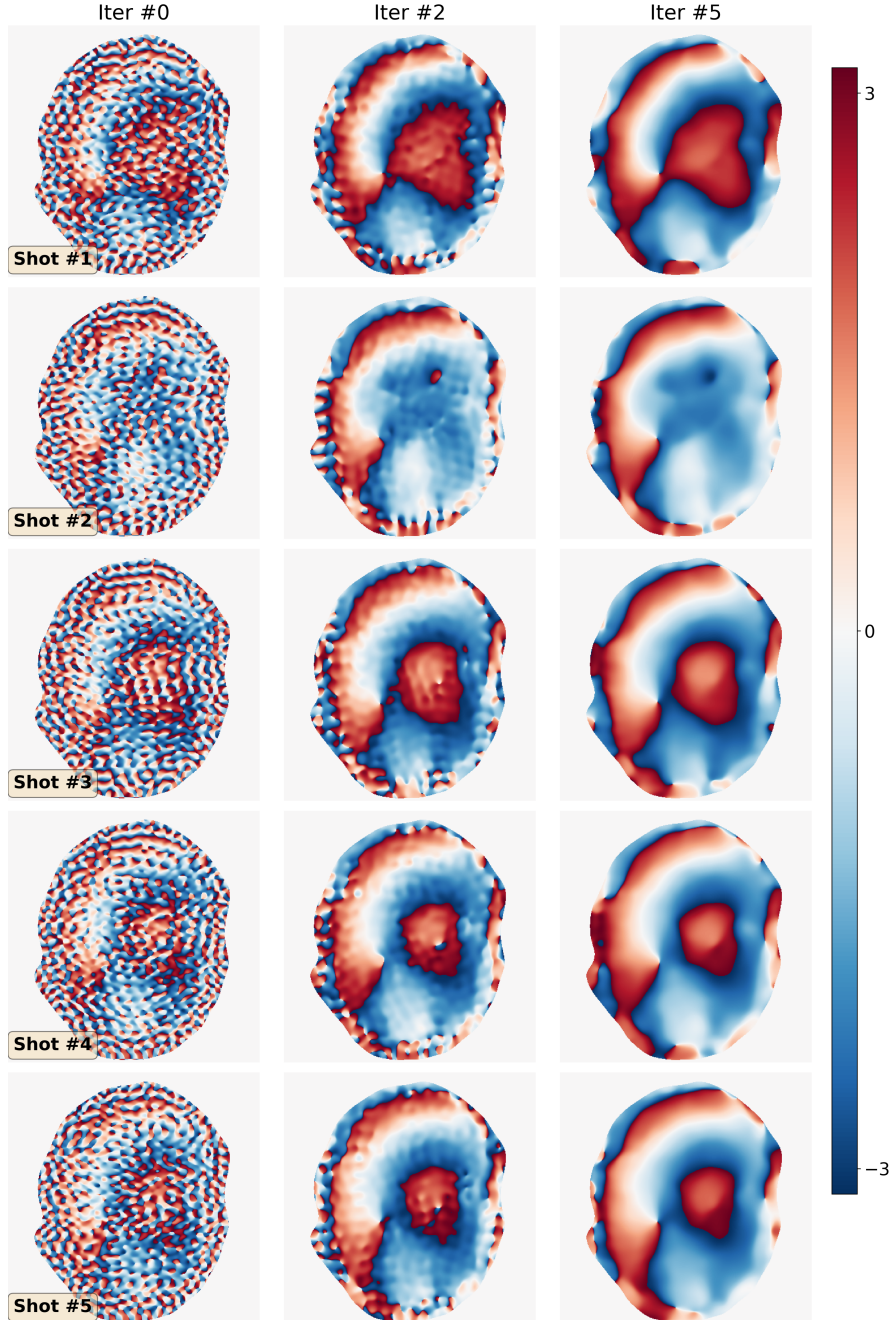


Figure 3: Iterative smoothing of shot-to-shot phase variation according to Eq. (6). Navigators from Protocol #3 were reconstructed based on Step I in Section 2.5 and then used as the input (iter #0, left column).

8th DW image from 4-shot iEPI @ 1 mm ISO

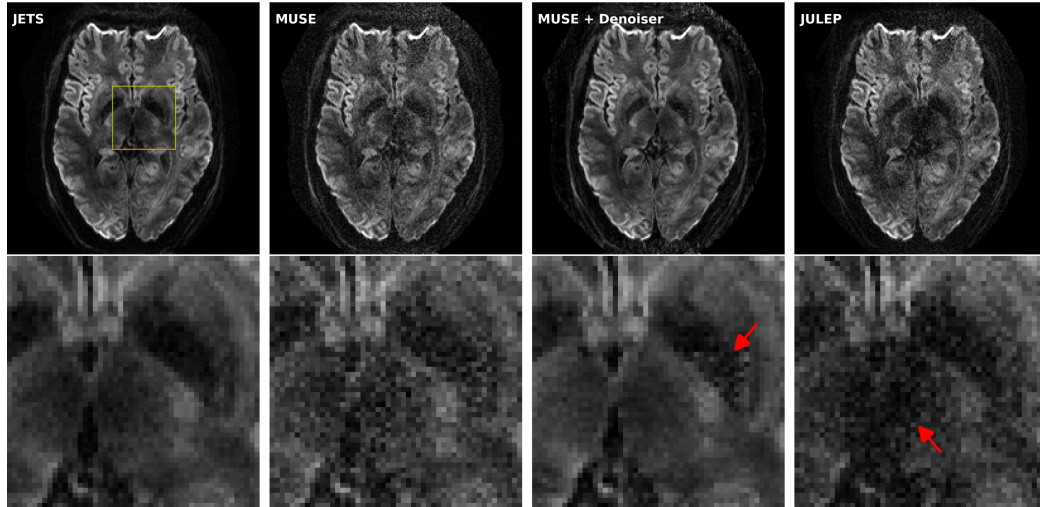


Figure 4: Reconstructed DW images (the 8th diffusion encoding) based on 4-shot iEPI acquisition with 1 mm isotropic resolution (Protocol #1 in Table 1). Four reconstruction methods are compared (from left to right): JETS, MUSE, MUSE with denoiser, and JULEP. The 2nd row displays the magnified views of the yellow square. The image from the denoiser (3rd column) shows residual noise patterns within the globus pallidus (indicated by the red arrow). The JULEP reconstruction (4th column) shows signal dropout in the central region (indicated by the red arrow).

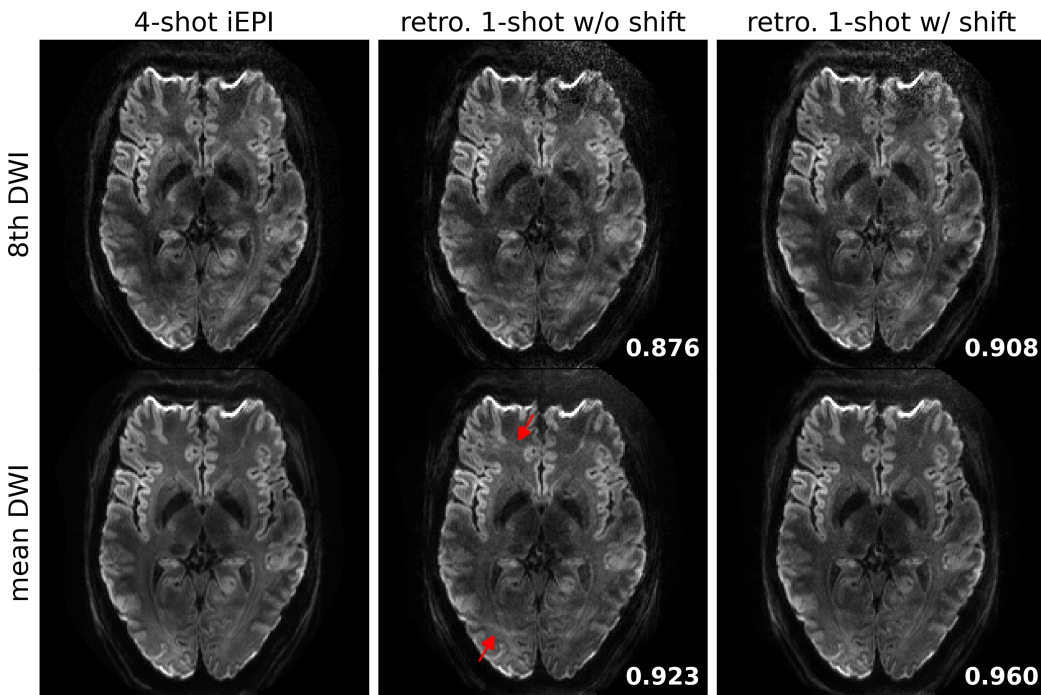


Figure 5: Quantitative validation of the proposed k_y -shift encoding sampling pattern based on 4-shot iEPI acquisition with 1 mm isotropic resolution (Protocol #1 in Table 1). (Top) the 8th diffusion encoding and (bottom) mean DWI over 20 diffusion encodings. (1st column) JETS reconstruction of 4-shot iEPI acquisition is used as the ground truth. The 2nd and the 3rd column displays JETS reconstruction of retrospectively undersampled 1-shot acquisition without and with k_y shifting, respectively. Residual aliasing artifacts are visible in the reconstruction without k_y shifting, as indicated by the red arrows. Structural similarity (SSIM) values are computed and displayed in the bottom right corners.

283 *3.3. Retrospectively undersampling from the four-shot iEPI acquisition*

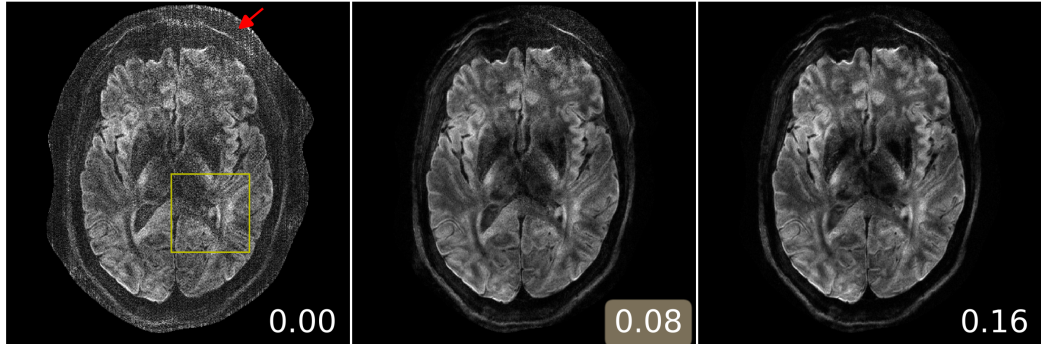
284 JETS reconstruction results on the four-shot prospectively fully-sampled
285 data from Protocol #1 in Table 1, as well as on the retrospectively under-
286 sampled one-shot data without and with the proposed k_y shift are displayed
287 in Fig. 5. Residual aliasing artifacts are visible in the reconstruction with-
288 out k_y shifting, as indicated by the red arrows. In contrast, the k_y shifting
289 scheme supplies a complementary k - q -space sampling pattern, which is bene-
290 ficial for joint reconstructions such as JETS. As shown in Fig. 5, JETS results
291 in improved SSIM values and reduced aliasing artifacts, when compared to
292 the reconstruction without k_y shifting. Figs. 4 and 5 show a slice containing R990.7
293 the globus pallidus with strong T_2 -weighted contrast and highlighting the
294 advantage of k_y -shift encoding in reducing undersampling artifacts.

295 *3.4. Analysis of reconstruction parameters*

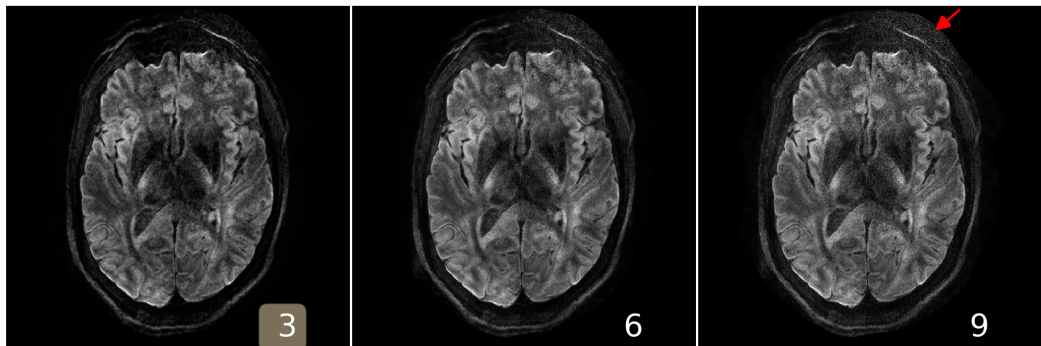
296 Here we provide a systematic analysis of the proposed JETS reconstruc-
297 tion with LLR regularization applied to the spatial-diffusion dimension, as
298 shown in Fig. 6.

299 First, we varied the regularization strength λ . We tested values of 0, 0.08,
300 and 0.16. The reconstruction with $\lambda = 0$ in Eq. (7) corresponds to parallel
301 imaging reconstruction without LLR regularization. It is worth noting that
302 the proposed NAViEPI sequence demonstrates high-quality sub-millimeter
303 DW images ($0.5 \times 0.5 \times 2.0 \text{ mm}^3$ in this example). The DW images can be
304 further improved with the use of LLR regularization, i.e., reduced noise, as
305 seen in the reconstruction with $\lambda = 0.08$. Increasing λ (e.g. 0.16) further
306 reduces noise, but at the cost of increased blurring. Therefore, $\lambda = 0.08$ was
307 selected in this work.

(A) varying λ , keeping block as 6 and stride as 1



(B) varying block width, keeping λ 0.08 and stride 1



(C) varying stride, keeping λ as 0.08 and block as 6

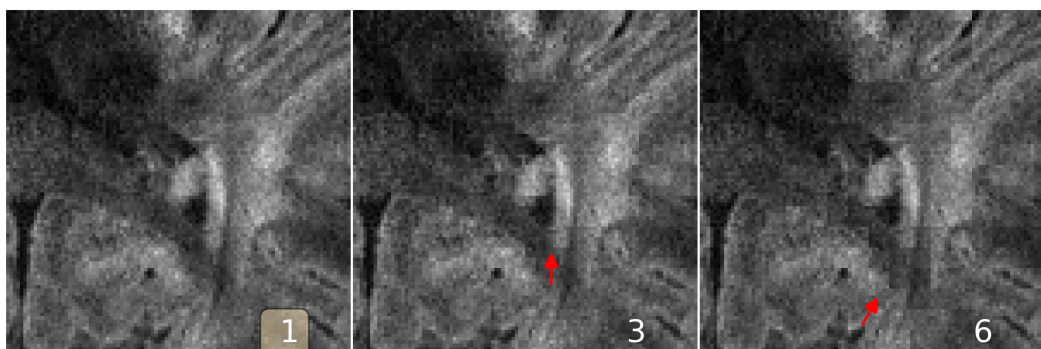


Figure 6: Analysis of reconstruction parameters based on the 3-scan trace acquisition with $0.5 \times 0.5 \times 2.0 \text{ mm}^3$ (Protocol #3 in Table 1). Displayed are JETS reconstructed single-direction DW images. (A) Varying the regularization strength λ from 0 to 0.08 and 0.16. (B) Varying the block width from 3 to 6 and 9. The red arrow indicates increased noise with the large block width. (C) Varying the stride size from 1 to 3 (partially overlapping) and 6 (non-overlapping). The red arrows indicate blocky artifacts.

308 Second, besides the regularization strength, the block size (i.e., the area
309 of 2D patches) also plays a role in denoising. We employed square blocks in R990.4.a
310 this work. Here, **the block width** of 3 shows the best denoising as compared
311 to 6 and 9, especially in the peripheral brain region.

312 Third, we varied the stride, i.e., the step from one local patch to the
313 next. The use of overlapping LLR (Fig. 6 (C) left) better suppresses blocky
314 artifacts, compared to **the partially overlapping (stride < block)** LLR (Fig. 6
315 (C) middle) and **the non-overlapping (stride = block)** LLR (Fig. 6 (C) right). R990.4.b

316 *3.5. Sampling efficiency of NAViEPI*

317 As shown in Fig. 7, NAViEPI achieves sub-millimeter resolution (voxel
318 size $0.5 \times 0.5 \times 2.0 \text{ mm}^3$) with the use of a 5-shot acquisition. When compared
319 to a single-shot acquisition with the same voxel size, the acquisition time of
320 NAViEPI is about two times longer, but the image quality of NAViEPI is
321 remarkably improved.

322 In the sub-millimeter imaging scenario, the increased base resolution re-
323 quires longer TE (143 ms) in the single-shot acquisition, which results in
324 significant signal loss due to T_2 relaxation. Therefore, sub-millimeter DWI
325 necessitates multi-shot acquisition, which is subject to shot-to-shot phase
326 variation and long scan time. However, NAViEPI solves both challenges. The
327 5-shot acquisition reduces TE to 58 ms, and thus retains SNR significantly
328 compared to the single-shot acquisition. Moreover, the JETS reconstruction
329 can help to reduce noise and improve structural visibility.

330 Fig. 8 shows the JETS reconstructed b_0 and TRACE images in different
331 slice locations. Admittedly, the lower brain region (e.g. slice #22) exhibits in-
332 homogeneous and lower signal intensity than the upper slices. Such inhomogeneity

3-scan trace acquisition with voxel size $0.5 \times 0.5 \times 2.0 \text{ mm}^3$

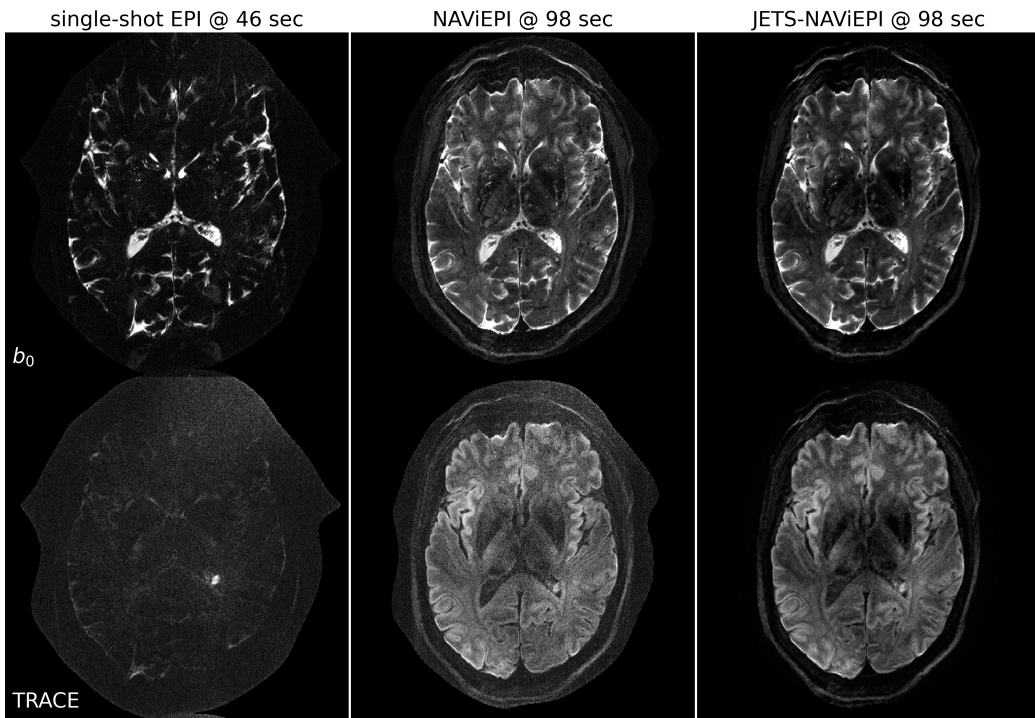


Figure 7: Sampling efficiency of the proposed NAViEPI sequence. 5-shot NAViEPI acquisition with the voxel size $0.5 \times 0.5 \times 2.0 \text{ mm}^3$ (Protocol #3) was compared with single-shot EPI acquisition (Protocol #4). Both the 1st and the 2nd columns were reconstructed via parallel imaging without LLR regularization, whereas the 3rd column was reconstructed via JETS.

3-scan trace acquisition with voxel size $0.5 \times 0.5 \times 2.0 \text{ mm}^3$

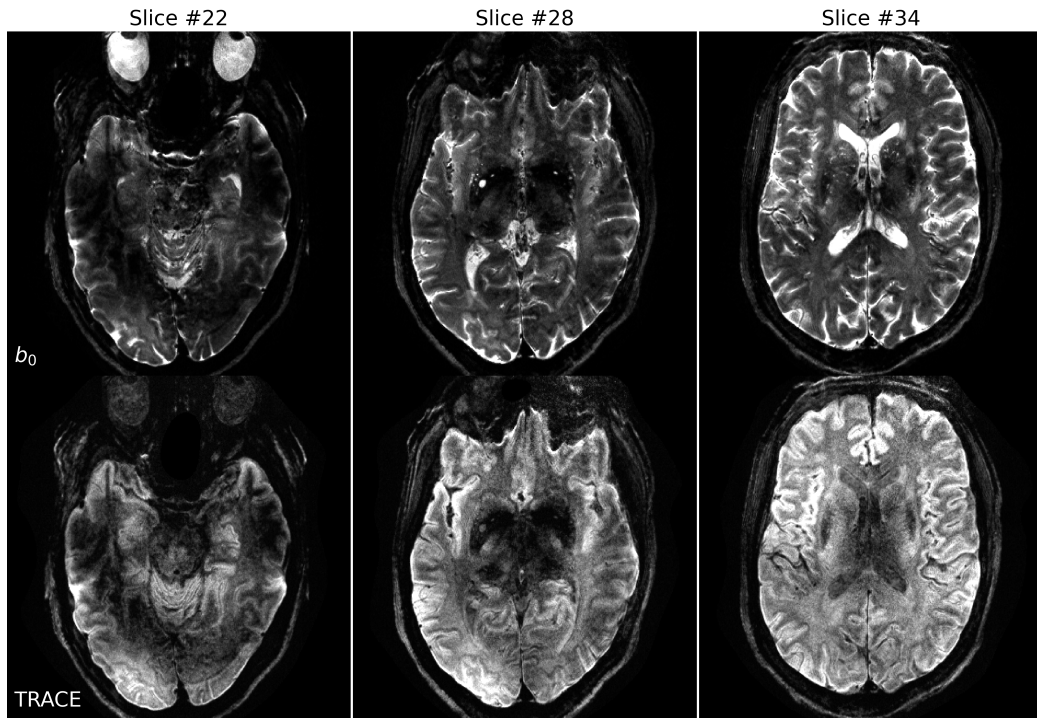


Figure 8: Reconstruction of the 3-scan trace acquisition with the voxel size $0.5 \times 0.5 \times 2.0 \text{ mm}^3$ (Protocol #3) at different slices.

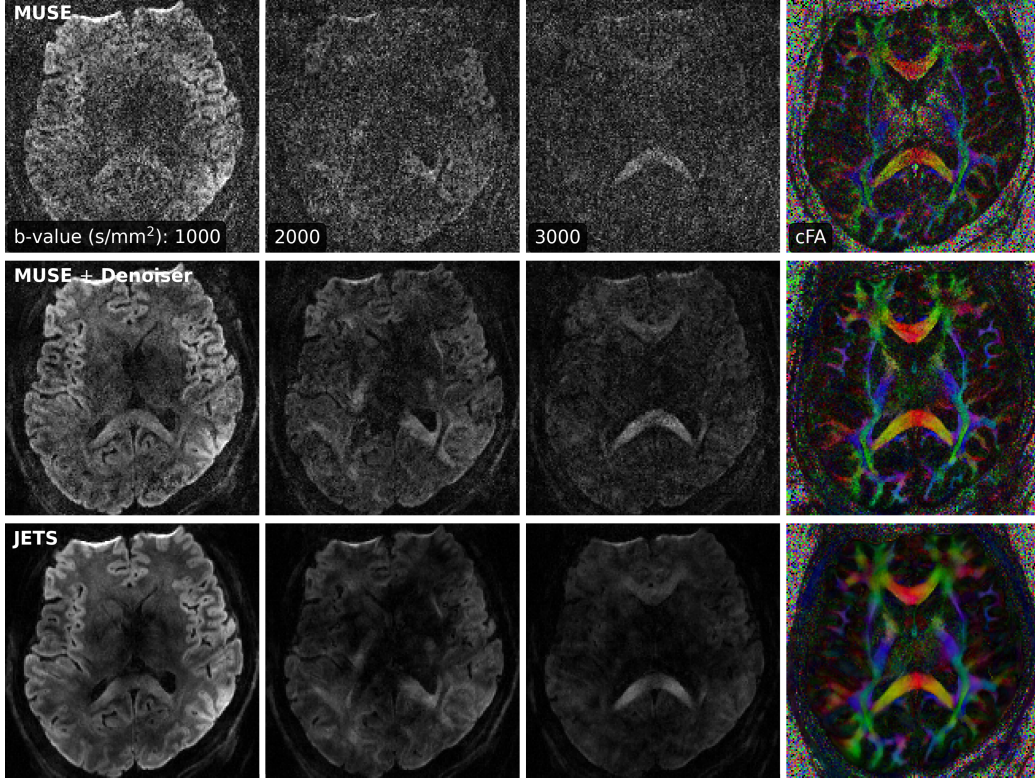


Figure 9: Comparison of three-shell DWIs and cFA maps with data acquired by Protocol #2 in Table 1. Reconstruction methods from top to bottom were MUSE, MUSE with the local-PCA denoiser, and the proposed JETS method.

333 geneity can be alleviated with the use of multi-channel parallel transmission
 334 (Katscher et al., 2003; Grissom et al., 2010).

335 Here, Figs. 6 and 7 select a slice with a benign lesion (the circular bright R990.7
 336 spot) within the left ventricle. Fig. 8 displays three representative slices: (left)
 337 the lower brain region which identifies the B_1^+ field inhomogeneity, (middle)
 338 the middle brain slice which shows susceptibility artifacts in the frontal re-
 339 gion, and (right) the upper brain slice which shows the ventricle.

340 *3.6. Diffusion tensor imaging*

341 Protocol #2 in Table 1 yields an acceleration factor of 6×3 per shot, re-
342 sulting in severe noise amplification in MUSE reconstructed DWIs, as shown
343 in Fig. 9. Here, a slice that highlights the corpus callosum is displayed, and R990.7
344 the diffusion direction at the b -value of 3000 s/mm^2 with bright signal within
345 the corpus callosum is shown. The local-PCA denoiser substantially removes
346 noise, but the DWI at high b -values still illustrates more noise, compared to
347 the proposed JETS reconstruction.

348 **4. Discussion**

349 This work reports a novel DW-MRI technique, JETS-NAViEPI. NAViEPI
350 (1) achieves the fast and efficient acquisition of both imaging and navigator
351 echoes, (2) enforces consistent effective ESP between the two echoes, and (3)
352 allows for undersampled iEPI as well as a large number of shots. Moreover,
353 compared to the single-shot acquisition, joint k - q -slice reconstruction with k_y -
354 shift encoding on NAViEPI retains SNR and reduces aliasing artifacts in DW
355 images. As a result, JETS-NAViEPI renders high spatiotemporal resolution
356 diffusion MRI protocols in 7 T, e.g., a 3-scan trace acquisition with the voxel
357 size $0.5 \times 0.5 \times 2.0 \text{ mm}^3$ at 1.5 min.

358 One limitation of JETS-NAViEPI is the long reconstruction time due to
359 the simultaneous reconstruction of all DW images and the use of overlapping
360 locally low-rank regularization. The reconstruction for the Protocol #3 in
361 Table 1 on an A100 GPU takes about 2 min per multi-band slice. To reduce
362 the computation time, coil compression algorithms (Buehrer et al., 2007;
363 Huang et al., 2008) can be employed to reduce the number of coils for image
364 reconstruction. Moreover, one can deploy multi-GPU distributed computing
365 or modern optimization algorithms (e.g. stochastic gradient descent) (Ong
366 et al., 2020) to speed up the reconstruction.

367 Neither the signal modeling in Eqs. (2) and (4) nor the LLR regulariza-
368 tion considers the subject motion. In the presence of motion, the regularized
369 reconstruction can degrade. To overcome this problem, scout-informed mo-
370 tion estimation and reconstruction (Polak et al., 2022) could be integrated
371 into the framework.

372 Another potential extension of this work is to incorporate distortion cor-

373 rection. The standard distortion correction method is known as TOPUP
374 (Andersson et al., 2003), which acquires two scans with opposing phase-
375 encoding directions to obtain the field inhomogeneity map and then per-
376 forms conjugate phase reconstruction to correct for distortion. Alternatively, R989.4,
377 a multi-echo acquisition could be used for the coil sensitivity reference scan, R990.13
378 such that both coil sensitivity and B_0 field inhomogeneity maps could be
379 reconstructed from the data.

380 This work employed a single regularization weight λ to enforce low rank-
381 ness along the spatial-diffusion direction. However, SNR may be heteroge-
382 neous within the FOV. Therefore, one single regularization scalar may be
383 inadequate to cover the whole FOV. Beyond this SVT-based reconstruction,
384 one can seek to use machine learning to learn a q -space prior as the regularizer
385 (Hammernik et al., 2018; Lam et al., 2019; Mani et al., 2021).

386 Although NAViEPI employs navigators for the acquisition of shot-to-
387 shot phase variation, it is worth noting that phase behavior depends on
388 several hard-to-control factors such as pulsatile motion, bulk motion, loca-
389 tions within the brain, and diffusion sensitization strength. Therefore, more
390 comprehensive modeling or post-processing such as image registration can
391 be considered in future work.

392 This work compared LLR regularized JETS to MUSE post-processed by
393 the local PCA denoiser (Cordero-Grande et al., 2019). Both the LLR reg-
394 ularization and the local PCA denoiser are based on the principle that low
395 rankness exists in the spatial-diffusion dimension, where the spatial content
396 is extracted from local patches within the full image volume and the diffusion
397 dimension is from the q -space encoding. Both of them demonstrate effective
R990.3.b.2

398 denoising capabilities and allow for high-quality DW-MRI image reconstruc-
399 tion from the accelerated acquisition.

400 Technically, the LLR regularization is realized by soft thresholding of
401 the singular values of the spatial-diffusion matrices, whereas the denoiser
402 performs hard thresholding. Both approaches demonstrate effective noise
403 removal. In the scenario of accelerated acquisitions, one can employ both
404 approaches to maximally boost SNR, i.e., the use of LLR regularization for
405 image reconstruction followed by the denoiser as a post-processing step.

406 While this work reconstructs all DW images and then performs model
407 fitting, an alternative approach is to directly estimate b_0 and diffusion ten-
408 sors from measured k - q -space data using model-based reconstruction (Knoll
409 et al., 2015; Dong et al., 2018; Shafieizargar et al., 2023). Compared to DW
410 image reconstruction, model-based reconstruction solves for a fewer number
411 of unknowns, but requires strict diffusion tensor modeling and the use of
412 nonlinear least square solvers.

413 **5. Conclusions**

414 We demonstrated the JETS-NAViEPI technique, which integrates a k_y -
415 shifted encoding navigator-based interleaved EPI sequence and joint recon-
416 struction with overlapping locally low-rank regularization for high spatial-
417 angular-temporal resolution DW-MRI at 7 T. This technique allows for high-
418 quality DW image reconstruction with accelerated acquisitions.

419 **Funding**

420 Funding by the German Research Foundation (DFG) is gratefully ac-
421 knowledged (projects 513220538, 512819079; and project 500888779 of the
422 RU5534 MR biosignatures at UHF). In addition, funding by the National
423 Institutes of Health (NIH), R01 EB024532 and P41 EB017183, is gratefully
424 acknowledged.

425 **Data and code available statement**

426 In the spirit of reproducible and open science, we publish our source
427 code (<https://github.com/ZhengguoTan/sigpy>) as well as the raw k -space
428 data (<https://doi.org/10.5281/zenodo.7548595>). We also provide inter-
429 active demonstrations of the reconstruction procedure (https://github.com/ZhengguoTan/demo_jets_diffusion_mri_7t).
430

431 **Acknowledgments**

432 The authors gratefully acknowledge the scientific support and HPC re-
433 sources provided by the Erlangen National High Performance Computing
434 Center (NHR@FAU) of Friedrich-Alexander-Universität Erlangen-Nürnberg
435 (FAU) under the NHR project b143dc. NHR funding is provided by federal
436 and Bavarian state authorities. NHR@FAU hardware is partially funded by
437 the German Research Foundation (DFG) – 440719683.

438 The authors thank Dr. Peter Neher for the discussion on MITK-Diffusion.
439 The authors thank Dr. Berkin Bilgic for making the MUSSELS source code
440 (<https://bit.ly/2QgBg9U>) publically available, Dr. Erpeng Dai for sharing
441 the JULEP source code (<https://github.com/daiexp/JULEP>) on GitHub,

442 and Dr. Zhiyong Zhang for sharing the SPA-LLR source code ([https://
443 github.com/ZZgroupSJTU/PMCmsDTI](https://github.com/ZZgroupSJTU/PMCmsDTI)) on GitHub. The authors also thank
444 Dr. Philipp Ehses for the discussion on twixtools ([https://github.com/
445 pehses/twixtools](https://github.com/pehses/twixtools)).

446 **References**

- 447 Andersson, J.L.R., Skare, S., Ashburner, J., 2003. How to correct suscepti-
448 bility distortions in spin-echo echo-planar images: application to diffusion
449 tensor imaging. NeuroImage 20, 870–888. doi:[10.1016/S1053-8119\(03\)
450 00336-7](https://doi.org/10.1016/S1053-8119(03)00336-7).
- 451 Bammer, R., Keeling, S.L., Augustin, M., Pruessmann, K.P., Wolf, R., Stoll-
452 berger, R., Hartung, H.P., Fazekas, F., 2001. Improved diffusion-weighted
453 single-shot echo-planar imaging (EPI) in stroke using sensitivity encoding
454 (SENSE). Magn. Reson. Med. 46, 548–554. doi:[10.1002/mrm.1226](https://doi.org/10.1002/mrm.1226).
- 455 Basser, P.J., Mattiello, J., Le Bihan, D., 1994. MR diffusion tensor
456 spectroscopy and imaging. Biophys. J. 66, 259–267. doi:[10.1016/
457 S0006-3495\(94\)80775-1](https://doi.org/10.1016/S0006-3495(94)80775-1).
- 458 Bilgic, B., Chatnuntawech, I., Manhard, M.K., Tian, Q., Liao, C., Iyer, S.S.,
459 Cauley, S.F., Huang, S.Y., Polimeni, J.R., Wald, L.L., Setsompop, K.,
460 2019. Highly accelerated multishot echo planar imaging through synergistic
461 machine learning and joint reconstruction. Magn. Reson. Med. 82, 1343–
462 1358. doi:[10.1002/mrm.27813](https://doi.org/10.1002/mrm.27813).
- 463 Block, K.T., Uecker, M., Frahm, J., 2007. Undersampled radial MRI with

- 464 multiple coils. Iterative image reconstruction using a total variation con-
465 straint. Magn. Reson. Med. 57, 1186–1098. doi:[10.1002/mrm.21236](https://doi.org/10.1002/mrm.21236).
- 466 Boyd, S., Parikh, N., Chu, E., Peleato, B., Eckstein, J., 2010. Distributed
467 optimization and statistical learning via the alternating direction method
468 of multipliers. Foundations and Trends in Machine Learning 3, 1–122.
469 doi:[10.1561/2200000016](https://doi.org/10.1561/2200000016).
- 470 Breuer, F.A., Blaimer, M., Heidemann, R.M., Mueller, M.F., Griswold, M.A.,
471 Jakob, P.M., 2005. Controlled aliasing in parallel imaging results in higher
472 acceleration (CAPIRINHA) for multi-slice imaging. Magn. Reson. Med.
473 53, 684–691. doi:[10.1002/mrm.20401](https://doi.org/10.1002/mrm.20401).
- 474 Buehrer, M., Pruessmann, K.P., Boesiger, P., Kozerke, S., 2007. Array com-
475 pression for MRI with large coil arrays. Magn. Reson. Med 57, 1131–1139.
476 doi:[10.1002/mrm.21237](https://doi.org/10.1002/mrm.21237).
- 477 Butts, K., Riederer, S.J., Ehman, R.L., Thompson, R.M., Jack, C.R., 1993.
478 Interleaved echo planar imaging on a standard MRI system. Magn. Reson.
479 Med. 31, 67–72. doi:[10.1002/mrm.1910310111](https://doi.org/10.1002/mrm.1910310111).
- 480 Cai, J.F., Candès, E.J., Shen, Z., 2010. A singular value threshold-
481 ing algorithm for matrix completion. SIAM. J. Optim. 20, 1956–1982.
482 doi:[10.1137/080738970](https://doi.org/10.1137/080738970).
- 483 Chen, N.K., Guidon, A., Chang, H.C., Song, A.W., 2013. A robust multi-
484 shot scan strategy for high-resolution diffusion weighted MRI enabled by
485 multiplexed sensitivity-encoding (MUSE). NeuroImage 72, 41–47. doi:[10.1016/j.neuroimage.2013.01.038](https://doi.org/10.1016/j.neuroimage.2013.01.038).

- 487 Cordero-Grande, L., Christiaens, D., Hutter, J., Price, A.N., Hajnal, J.V.,
488 2019. Complex diffusion-weighted image estimation via matrix recovery
489 under general noise models. NeuroImage 200, 391–404. doi:[10.1016/j.neuroimage.2019.06.039](https://doi.org/10.1016/j.neuroimage.2019.06.039).
- 491 Dai, E., Ma, X., Zhang, Z., Yuan, C., Guo, H., 2017. Simultaneous multislice
492 accelerated interleaved EPI DWI using generalized blipped-CAIPI acqui-
493 sition and 3D K-space reconstruction. Magn. Reson. Med. 77, 1593–1605.
494 doi:[10.1002/mrm.26249](https://doi.org/10.1002/mrm.26249).
- 495 Dai, E., Mani, M., McNab, J.A., 2023. Multi-band multi-shot diffu-
496 sion MRI reconstruction with joint usage of structured low-rank con-
497 straints and explicit phase mapping. Magn. Reson. Med. 89, 95–111.
498 doi:[10.1002/mrm.29422](https://doi.org/10.1002/mrm.29422).
- 499 Dai, E., Zhang, Z., Ma, X., Dong, Z., Li, X., Xiong, Y., Yuan, C., Guo, H.,
500 2018. The effects of navigator distortion and noise level on interleaved EPI
501 DWI reconstruction: a comparison between image- and *k*-space method.
502 Magn. Reson. Med. 80, 2024–2032. doi:[10.1002/mrm.27190](https://doi.org/10.1002/mrm.27190).
- 503 Dong, Z., Dai, E., Wang, F., Zhang, Z., Ma, X., Yuan, C., Guo, H., 2018.
504 Model-based reconstruction for simultaneous multislice and parallel imag-
505 ing accelerated multishot diffusion tensor imaging. Med. Phys. 45, 3196–
506 3204. doi:[10.1002/mp.12974](https://doi.org/10.1002/mp.12974).
- 507 Garyfallidis, E., Brett, M., Amirbekian, B., Rokem, A., van der Walt, S.,
508 Descoteaux, M., Nimmo-Smith, I., Contributors, D., 2014. DIPY, a library

- 509 for the analysis of diffusion MRI data. *Front. Neuroinform.* 8, 1–17. doi:[10.3389/fninf.2014.00008](https://doi.org/10.3389/fninf.2014.00008).
- 510
- 511 Grissom, W.A., Sacolick, L., Vogel, M.W., 2010. Improving high-field MRI
512 using parallel excitation. *Imaging Med.* 2, 675–693. doi:[10.2217/IIM.10.62](https://doi.org/10.2217/IIM.10.62).
- 513
- 514 Griswold, M.A., Jakob, P.M., Heidemann, R.M., Nittka, M., Jellus, V.,
515 Wang, J., Kiefer, B., Haase, A., 2002. Generalized autocalibrating par-
516 tially parallel acquisitions (GRAPPA). *Magn. Reson. Med.* 47, 1202–1210.
517 doi:[10.1002/mrm.10171](https://doi.org/10.1002/mrm.10171).
- 518
- 519 Guhaniyogi, S., Chu, M.L., Chang, H.C., Song, A.W., Chen, N.K., 2016. Mo-
520 tion immune diffusion imaging using augmented MUSE for high-resolution
521 multi-shot EPI. *Magn. Reson. Med.* 75, 639–652. doi:[10.1002/mrm.25624](https://doi.org/10.1002/mrm.25624).
- 522
- 523 Hammernik, K., Klatzer, T., Kobler, E., Recht, M.P., Sodickson, D.K., Pock,
524 T., Knoll, F., 2018. Learning a variational network for reconstruction of
525 accelerated MRI data. *Magn. Reson. Med.* 79, 3055–3071. doi:[10.1002/mrm.26977](https://doi.org/10.1002/mrm.26977).
- 526
- 527 Heidemann, R.M., Porter, D.A., Anwander, A., Feiweier, T., Heberlein, K.,
528 Knösche, T.R., Turner, R., 2010. Diffusion imaging in humans at 7 T
529 using readout-segmented EPI and GRAPPA. *Magn. Reson. Med.* 64, 9–
530 14. doi:[10.1002/mrm.22480](https://doi.org/10.1002/mrm.22480).
- 531
- 532 Hestenes, M.R., Stiefel, E., 1952. Methods of conjugate gradients for solving
533 linear systems. *J. Res. Natl. Bur. Stand.* 49, 409–436. doi:[10.6028/jres.049.044](https://doi.org/10.6028/jres.049.044).

- 532 Hu, Y., Wang, X., Tian, Q., Yang, G., Daniel, B., McNab, J., Hargreaves, B.,
533 2020. Multi-shot diffusion-weighted MRI reconstruction with magnitude-
534 based spatial-angular locally low-rank regularization (SPA-LLR). *Magn.*
535 *Reson. Med.* 83, 1596–1607. doi:[10.1002/mrm.28025](https://doi.org/10.1002/mrm.28025).
- 536 Huang, F., Vijayakumar, S., Li, Y., Hertel, S., Duensing, G.R., 2008. A soft-
537 ware channel compression technique for faster reconstruction with many
538 channels. *Magn. Reson. Imaging* 26, 133–141. doi:[10.1016/j.mri.2007.04.010](https://doi.org/10.1016/j.mri.2007.04.010).
- 540 Jeong, H.K., Gore, J.C., Anderson, A.W., 2013. High-resolution human
541 diffusion tensor imaging using 2-D navigated multishot SENSE EPI at 7
542 T. *Magn. Reson. Med.* 69, 793–802. doi:[10.1002/mrm.24320](https://doi.org/10.1002/mrm.24320).
- 543 Jones, D.K., 2010. Diffusion MRI: Theory, methods, and applications. Oxford
544 University Press. doi:[10.1093/med/9780195369779.001.0001](https://doi.org/10.1093/med/9780195369779.001.0001).
- 545 Katscher, U., Börnert, P., Leussler, C., van den Brink, J.S., 2003. Transmit
546 SENSE. *Magn. Reson. Med.* 49, 144–150. doi:[10.1002/mrm.10353](https://doi.org/10.1002/mrm.10353).
- 547 Knoll, F., Raya, J.G., Halloran, R.O., Baete, S., Sigmund, E., Bammer, R.,
548 Block, T., Otazo, R., Sodickson, D.K., 2015. A model-based reconstruction
549 for undersampled radial spin-echo DTI with variational penalties on the
550 diffusion tensor. *NMR Biomed* 28, 353–366. doi:[10.1002/nbm.3258](https://doi.org/10.1002/nbm.3258).
- 551 Lam, F., Li, Y., Peng, X., 2019. Constrained magnetic resonance spectro-
552 scopic imaging by learning nonlinear low-dimensional models. *IEEE Trans.*
553 *Med. Imaging* 39, 545–555. doi:[10.1109/TMI.2019.2930586](https://doi.org/10.1109/TMI.2019.2930586).

- 554 Le Bihan, D., Breton, E., Lallemand, D., Grenier, P., Cabanis, E., Laval-
555 Jeantet, M., 1986. MR imaging of intravoxel incoherent motions: appli-
556 cation to diffusion and perfusion in neurologic disorders. Radiology 161,
557 401–407. doi:[10.1148/radiology.161.2.3763909](https://doi.org/10.1148/radiology.161.2.3763909).
- 558 Liang, Z.P., 2007. Spatiotemporal imaging with partially separable functions,
559 in: 2007 4th IEEE International Symposium on Biomedical Imaging: From
560 Nano to Macro, pp. 988–991. doi:[10.1109/ISBI.2007.357020](https://doi.org/10.1109/ISBI.2007.357020).
- 561 Liu, C., Moseley, M.E., Bammer, R., 2005. Simultaneous phase cor-
562 rection and SENSE reconstruction for navigated multi-shot DWI with
563 non-Cartesian k -space sampling. Magn. Reson. Med. 54, 1412–1422.
564 doi:[10.1002/mrm.20706](https://doi.org/10.1002/mrm.20706).
- 565 Lustig, M., Donoho, D., Pauly, J.M., 2007. Sparse MRI: The application of
566 compressed sensing for rapid MR imaging. Magn. Reson. Med. 58, 1182–
567 1195. doi:[10.1002/mrm.21391](https://doi.org/10.1002/mrm.21391).
- 568 Mani, M., Jacob, M., Kelley, D., Magnotta, V., 2017. Multi-shot sensitivity-
569 encoded diffusion data recovery using structured low-rank matrix comple-
570 tion (MUSSELS). Magn. Reson. Med. 78, 494–507. doi:[10.1002/mrm.26382](https://doi.org/10.1002/mrm.26382).
- 572 Mani, M., Magnotta, V.A., Jacob, M., 2021. qModeL: A plug-and-play
573 model-based reconstruction for highly accelerated multi-shot diffusion MRI
574 using learned priors. Magn. Reson. Med. 86, 835–851. doi:[10.1002/mrm.28756](https://doi.org/10.1002/mrm.28756).

- 576 Mansfield, P., 1977. Multi-planar image formation using NMR spin echoes.
577 J Phys C 10, 55–58. doi:[10.1088/0022-3719/10/3/004](https://doi.org/10.1088/0022-3719/10/3/004).
- 578 Maudsley, A.A., 1980. Multiple-line-scanning spin density imaging. J. Magn.
579 Reson. 41, 112–126. doi:[10.1016/0022-2364\(80\)90207-3](https://doi.org/10.1016/0022-2364(80)90207-3).
- 580 Merboldt, K.D., Hanicke, W., Frahm, J., 1985. Self-diffusion NMR imag-
581 ing using stimulated echoes. J. Magn. Reson. 64, 479–486. doi:[10.1016/0022-2364\(85\)90111-8](https://doi.org/10.1016/0022-2364(85)90111-8).
- 583 Mori, S., Crain, B.J., Chacko, V.P., Van Zijl, P.C.M., 1999. Three-
584 dimensional tracking of axonal projections in the brain by mag-
585 netic resonance imaging. Ann. Neurol. 45, 265–269. doi:[10.1002/1531-8249\(199902\)45:2<265::AID-ANA21>3.0.CO;2-3](https://doi.org/10.1002/1531-8249(199902)45:2<265::AID-ANA21>3.0.CO;2-3).
- 587 Ong, F., Lustig, M., 2019. SigPy: A Python package for high performance
588 iterative reconstruction, in: Proceedings of the 27th Annual Meeting of
589 ISMRM, Montréal, CAN, p. 4819. doi:[10.5281/zenodo.5893788](https://doi.org/10.5281/zenodo.5893788).
- 590 Ong, F., Zhu, X., Cheng, J.Y., Johnson, K.M., Larson, P.E.Z., Vasanawala,
591 S.S., Lustig, M., 2020. Extreme MRI: Large-scale volumetric dynamic
592 imaging from continuous non-gated acquisitions. Magn. Reson. Med. 84,
593 1763–1780. doi:[10.1002/mrm.28235](https://doi.org/10.1002/mrm.28235).
- 594 Pipe, J.G., Farthing, V.G., Forbes, K.P., 2002. Multishot diffusion-weighted
595 FSE using PROPELLER MRI. Magn. Reson. Med. 47, 42–52. doi:[10.1002/mrm.10014](https://doi.org/10.1002/mrm.10014).
- 597 Polak, D., Splitthoff, D.N., Clifford, B., Lo, W.C., Huang, S.Y., Conklin, J.,
598 Wald, L.L., Setsompop, K., Cauley, S., 2022. Scout accelerated motion

- 599 estimation and reduction (SAMER). Magn. Reson. Med. 87, 163–178.
600 doi:[10.1002/mrm.28971](https://doi.org/10.1002/mrm.28971).
- 601 Porter, D.A., Heidemann, R.M., 2009. High resolution diffusion-weighted
602 imaging using readout-segmented echo-planar imaging, parallel imaging
603 and a two-dimensional navigator-based reacquisition. Magn. Reson. Med.
604 62, 468–475. doi:[10.1002/mrm.22024](https://doi.org/10.1002/mrm.22024).
- 605 Pruessmann, K.P., Weiger, M., Scheidegger, M.B., Boesiger, P., 1999.
606 SENSE: Sensitivity encoding for fast MRI. Magn. Reson. Med. 42, 952–
607 962. doi:[10.1002/\(SICI\)1522-2594\(199911\)42:5<952::AID-MRM16>3.0.CO;2-S](https://doi.org/10.1002/(SICI)1522-2594(199911)42:5<952::AID-MRM16>3.0.CO;2-S).
- 608
- 609 Ra, J.B., Rim, C.Y., 1993. Fast imaging using subencoding data sets from
610 multiple detectors. Magn. Reson. Med. 30, 142–145. doi:[10.1002/mrm.1910300123](https://doi.org/10.1002/mrm.1910300123).
- 611
- 612 Roemer, P.B., Edelstein, W.A., Hayes, C.E., Souza, S.P., Mueller, O.M.,
613 1990. The NMR phased array. Magn. Reson. Med. 16, 192–225. doi:[10.1002/mrm.1910160203](https://doi.org/10.1002/mrm.1910160203).
- 614
- 615 Setsompop, K., Fan, Q., Stockmann, J., Bilgic, B., Huang, S., Cauley, S.F.,
616 Nummenmaa, A., Wang, F., Rathi, Y., Witzel, T., Wald, L.L., 2018. High-
617 resolution *in vivo* diffusion imaging of the human brain with generalized
618 slice dithered enhanced resolution: Simultaneous multislice (gSlider-SMS).
619 Magn. Reson. Med. 79, 141–151. doi:[10.1002/mrm.26653](https://doi.org/10.1002/mrm.26653).
- 620 Setsompop, K., Gagoski, B.A., Polimeni, J.R., Witzel, T., Wedeen, V.J.,
621 Wald, L.L., 2012. Blipped-controlled aliasing in parallel imaging for si-

- 622 multaneous multislice echo planar imaging with reduced *g*-factor penalty.
623 Magn. Reson. Med. 67, 1210–1224. doi:[10.1002/mrm.23097](https://doi.org/10.1002/mrm.23097).
- 624 Shafieizargar, B., Jeurissen, B., Poot, D.H.J., Klein, S., Van Audekerke,
625 J., Verhoye, M., den Dekker, A.J., Sijbers, J., 2023. ADEPT: Accurate
626 diffusion echo-planar imaging with multi-contrast shoTs. Magn. Reson.
627 Med. 89, 396–410. doi:[10.1002/mrm.29398](https://doi.org/10.1002/mrm.29398).
- 628 Tournier, J.D., Smith, R., Raffelt, D., Tabbara, R., Dhollander, T., Pietsch,
629 M., Christiaens, D., Jeurissen, B., Yeh, C.H., Connelly, A., 2019. MRtrix3:
630 A fast, flexible and open software framework for medical image processing
631 and visualisation. NeuroImage 202, 116137. doi:<https://doi.org/10.1016/j.neuroimage.2019.116137>.
- 633 Trzasko, J., Manduca, A., 2011. Local versus global low-rank promotion in
634 dynamic MRI series reconstruction, in: Proceedings of the 19th Annual
635 Meeting of ISMRM, Montréal, CAN, p. 4371.
- 636 Tuch, D.S., Reese, T.G., Wiegell, M.R., Makris, N., Belliveau, J.W., Wedeen,
637 V.J., 2002. High angular resolution diffusion imaging reveals intravoxel
638 white matter fiber heterogeneity. Magn. Reson. Med. 48, 577–582. doi:[10.1002/mrm.10268](https://doi.org/10.1002/mrm.10268).
- 640 Uecker, M., Lai, P., Murphy, M.J., Virtue, P., Elad, M., Pauly, J.M.,
641 Vasanawala, S.S., Lustig, M., 2014. ESPIRiT – an eigenvalue approach
642 to autocalibrating parallel MRI: Where SENSE meets GRAPPA. Magn.
643 Reson. Med. 71, 990–1001. doi:[10.1002/mrm.24751](https://doi.org/10.1002/mrm.24751).

- 644 Wu, W., Koopmans, P.J., Andersson, J.L., Miller, K.L., 2019. Diffusion
645 Acceleration with Gaussian process Estimated Reconstruction (DAGER).
646 Magn. Reson. Med. 82, 107–125. doi:[10.1002/mrm.27699](https://doi.org/10.1002/mrm.27699).
- 647 Wu, W., Miller, K.L., 2017. Image formation in diffusion MRI: A review
648 of recent technical developments. J. Magn. Reson. Imaging 46, 646–662.
649 doi:[10.1002/jmri.25664](https://doi.org/10.1002/jmri.25664).
- 650 Zhang, T., Pauly, J.M., Levesque, I.R., 2015. Accelerated parameter mapping
651 with a locally low rank constraint. Magn. Reson. Med. 73, 655–661. doi:[10.1002/mrm.25161](https://doi.org/10.1002/mrm.25161).